International Journal of Nanomedicine

Dovepress
Taylor & Francis Group

Open Access Full Text Article

ORIGINAL RESEARCH

Intravesical Tumor-Selective Mucoadhesive Hydrogel for Effective Chemotherapy In Murine Model

Bin Zheng[1,2,*], Zheng Chen[1,*], Luping Sun[1,*], Jing Quan[2], Jianwen Wei[1], Baoyuan Huang[1], Dahong Zhang[2], Pu Zhang[2], Yumin Zhuo[1]

[1]Department of Urology, The First Affiliated Hospital of Jinan University, Jinan University, Guangzhou, People's Republic of China; [2]Urology & Nephrology Center, Department of Urology, Zhejiang Provincial People's Hospital (Affiliated People's Hospital), Hangzhou Medical College, Hangzhou, Zhejiang, People's Republic of China

*These authors contributed equally to this work

Correspondence: Pu Zhang; Yumin Zhuo, Email zhangpuxjtuer@163.com; tzhuoyumin@126.com

---

Introduction: The therapeutic efficacy of intravesical agents for bladder cancer (BCa) is frequently constrained by their clearance via urine flushing and periodic bladder emptying, as well as the absence of tumor-targeting capabilities. Consequently, an effective drug delivery system must possess both tumor-targeting and adhesion properties to overcome these limitations.

Methods: In this study, we investigated a tumor-selective hydrogel as a potential vehicle for BCa treatment. For the first time in the field of intravesical therapy, we introduced the concept of pre-targeting, sequentially instilling modified polyarginine and membrane nanoparticles into the bladder to achieve selective gelation on the tumor surface. We comprehensively evaluated tumor selectivity, endocytosis pathways, organelle localization, and osmotic capacity, and demonstrated in vivo and in vitro degradation following drug delivery.

Results: The pre-targeted hydrogel exhibited superior tumor selectivity. The drug-loaded membrane nanoparticles released during hydrogel degradation were internalized by tumor cells at levels exceeding those in normal cells by more than eightfold. Our findings indicated that this internalization process was energy-dependent and mediated by caveolin. Post-internalization, the drug-loaded membrane nanoparticles localized to the endoplasmic reticulum and Golgi apparatus, with minimal colocalization with lysosomes. Moreover, the hydrogel demonstrated profound penetration into tumor tissue. In terms of antitumor efficacy, the hydrogel loaded with gemcitabine exhibited significantly enhanced therapeutic effects compared to free gemcitabine.

Conclusion: Our dual-functional hydrogel system exhibits robust anti-tumor activity against BCa, presenting a promising alternative for intravesical therapy. This innovative approach addresses key limitations of current treatments by combining tumor targeting with sustained drug adhesion, offering a novel strategy for the management of BCa.

Keywords: intravesical therapy, pretargeted drug delivery, tumor-selective, hydrogel, mucoadhesive

---

Introduction

Intravesical therapy (IT) is frequently employed post-transurethral resection of bladder tumors to prevent tumor recurrence and progression.[1–6] However, the efficacy of IT is compromised by urine washing, periodic voiding, and the mucosal barrier, which impede drug retention within the bladder.[7,8] While repeated IT is clinically recommended, its invasive nature renders it intolerable for many patients. Mucoadhesive vehicles, though capable of prolonged intravesical retention,[9–14] lack tumor-targeting specificity, potentially leading to severe complications such as cystitis, urinary tract infection, or bladder hemorrhage.[15]

Tumor-selective hydrogels (TsH) have emerged as promising agents, combining mucoadhesion with tumor-targeting capabilities. Concerns persist, however, regarding the reliability of their tumor-targeting mechanisms—primarily stimuli-

Received: 23 February 2025
Accepted: 19 May 2025
Published: 4 June 2025

responsive actions and tumor-selective ligand-receptor binding—in the complex bladder environment.[16,17] Dynamic urinary changes can obscure microenvironmental signals (eg, pH, ions, reactive oxygen species),[18–20] potentially deactivating stimuli-responsive hydrogels before they reach the tumor surface. Additionally, in one-step binding approaches, premature gelation may occur before effective tumor-targeting via ligand-receptor interactions is achieved.[21,22]

To address these challenges, we introduced the concept of pre-targeting into intravesical therapy, separating active tumor-targeting and gelation into distinct steps and ensuring their convergence exclusively on the tumor surface. Specifically, we first administered a mucoadhesive, bispecific pre-targeting ligand (R11-biotin) intravesically. This initial step directed the subsequent deposition of hydrogel precursors-comprising streptavidin-biotin-PEG-modified cell membrane nanovesicles (MN) and R11-biotin—onto the biotinylated tumor surface, achieving selective tumor gelation.[23] This strategy not only enhanced the anti-cancer efficacy of delivered gemcitabine (Gem) but also minimized off-target effects on healthy tissues.

Materials and Methods

R11 was purchased from SciLight Biotechnology Co. (China). Ethyl acetate, poly(lactic-co-glycolic acid) (PLGA) (Mw 38000–54,000), polyvinyl alcohol (PVA), Chlorpromazine(CPZ), filipin, aminoyl isopropyl ethyl ester (EIPA) and Streptavidin were obtained from Macklin BiochemicalCo., Ltd. (China). Gem was obtained from MedChemExpress. Biotin-PEG-NHS was purchased from Tanshtech(China). Cell Migration And Invasion Stain Kit(For Transwell) and artificial urine were obtained from Solarbio Life Science Co., Ltd. (China). Endoplasmic reticulum (ER) tracker, Golgi apparatus (GA) tracker, Lysosomes Tracker and the Cell Counting Kit-8 (CCK-8) was obtained from Yeasen Biotech Co., Ltd. (China). Potassium fluorescein was obtained from LABLEAD. Inc. (China).

The Preparation of Cell Membrane Fragment Extraction

T24 cells were harvested and lysed in Tris-HCl buffer (pH 7.4) containing 10 mm $MgCl_2$, 1× phenylmethylsulfonyl fluoride (PMSF), 0.2 mm EDTA, and phosphatase inhibitor cocktail (Roche), and the mixture was shaken overnight at 4°C. The cell suspension was sonicated three times with an ultrasonic probe at 20% amplitude for 20s each. Subsequent centrifugation steps included three cycles at 500 × g for 10 min at 4°C, followed by centrifugation at 10,000 × g for 30 min and finally at 70,000 × g for 90 min, all at 4°C. The resultant pellet, containing the cell membrane, was resuspended in PBS.[24]

Preparation of Nanoparticles and Tumor-Selective Hydrogel

The Gem loaded PLGA nanoparticles (PLGA-Gem) were prepared via the solvent evaporation method. Briefly, Gem (1 mg) and PLGA (10 mg) were dissolved in ethyl acetate (1 mL) and emulsified into ultrapure water under vigorous stirring. The resulting emulsion was added dropwise to a polyvinyl alcohol (PVA) solution (4 mL, 2.5 mg/mL) and sonicated (20 kHz, 30% amplitude, 30s). The organic solvent was evaporated at 25°C with stirring at 400 rpm for 12 h. The drug loading content (DLC) and drug loading efficiency (DLE) were calculated using the following equations: DLC (%) = $W_{(\text{drug in PLGA-Gem})}/\ W_{(\text{drug-loaded PLGA-Gem})} \times 100\%$; DLE (%) = $W_{(\text{drug in PLGA-Gem})}/\ W_{(\text{total feeding drug})} \times 100\%$. PLGA-Gem (1 mL, 1 mg/mL Gem) were mixed with T24 cell membrane fragments (0.3 mg) and processed using a microextruder equipped with a 400 nm polycarbonate filter. The resulting membrane-coated nanoparticles (M@PLGA-Gem) were washed and centrifuged at 14,000 × g for 30 min at 4°C. Biotinylation of M@PLGA-Gem was achieved by incubation with NHS-PEG-biotin (100 μL, 2 mmol/mL), followed by centrifugation to remove unbound NHS-PEG-biotin. R11 was similarly biotinylated using Sulfo-NHS-biotin. Finally, streptavidin was conjugated to biotinylated M@PLGA-Gem, and R11-biotin was added to form the hydrogel RM@PLGA-Gem.

Characterization of Hydrogel

The rheological properties of the hydrogel were evaluated using a 25-mm sandblasted parallel plate with a Peltier temperature-controlled system (Anton Parr MCR702 Rheometer). The particle size and zeta potential of PLGA-Gem and M@PLGA-Gem were measured via dynamic light scattering (DLS) using a Litesizer™ 500 (Anton Paar, Graz, Austria).

Nanoparticle stability was assessed by monitoring size changes in urine and PBS buffer. For scanning electron microscopy (SEM), the hydrogel was rapidly frozen in liquid nitrogen and sputter-coated with gold for 30 seconds. To simulate post-administration conditions in the bladder, mice with in situ bladder tumors were treated with RM@PLGA-Gem. After tumor resection, tissue samples (3 mm × 3 mm) were mounted on two parallel planks. One plank was fixed to a stainless steel base, while the other was connected to a lightweight plastic beaker via a pulley system. Water was added to the beaker at a rate of 1.0 mL/min, inducing gradual separation of the planks. The mucoadhesive force was determined by calculating the weight of the water-filled beaker at the point of separation.

Drug Release

The release rates of Gem from various formulations were evaluated in PBS buffer (pH 7.4) or urine at 37°C. Briefly, 2 mL of each formulation—PLGA-Gem, TM@PLGA-Gem, or RM@PLGA-Gem—at a Gem concentration of 1 mg/mL, were placed in dialysis bags (cutoff molecular weight: 3500 Da). These bags were subjected to shaking at 70 RPM in the respective liquid at 37°C. Samples were collected at predetermined intervals for HPLC analysis, with each data point measured in triplicate across three independent experiments. This approach ensures the accuracy and reproducibility of the release profile data.

Cell Culture

BCa cells (T24 and 5637) and SVHUC-1 (normal urothelium cells) were obtained from the National Collection of Authenticated Cell Cultures, China.

BCa Targeting Efficiency

To assess the targetability of the RM@PLGA-Gem nanoconjugate, T24, 5637, and SVHUC-1 cells were seeded into laser confocal petri dishes at a density of 5×10^4 cells per well. After incubation for 12 h, biotinylated R11 was incubated with SVHUC-1, T24, and 5637 cells for 45 min to allow binding. Subsequently, streptavidin-biotin-PEG-modified M@PLGA-cou6 (Gem was replaced by coumarin-6 at 2 mg/mL) was incubated with the cells for 2 h to facilitate selective labeling and visualization of the nanoconjugate binding. Cells were washed three times with pre-cooled PBS and stained with DAPI to visualize nuclear components. Confocal laser scanning microscopy (CLSM; Leica TCS SP5, Leica Microsystems, California, USA) was used to evaluate the targeting efficiency of the nanoconjugates in bladder cancer (BCa) cells. Quantitative analysis of the imaging data was performed using ImageJ software (NIH, Bethesda, MD, USA).

Endocytosis Pathway Determination

T24 and 5637 cells were seeded into laser confocal dishes at a density of 1×10^5 cells per dish. To investigate the endocytosis pathways, cells were pretreated with specific inhibitors: chlorpromazine hydrochloride (CPZ, 10 μg/mL), filipin (1 μg/mL), or ethyl isopropyl amiloride (EIPA, 10 μg/mL), each for 1 h. As a control, cells were also incubated at 4°C for 1 h to suppress energy-dependent endocytosis. Following pretreatment, biotinylated R11 and streptavidin-biotin-PEG-modified M@PLGA-cou6 (coumarin-6 replacing gemcitabine, 2 mg/mL) were co-incubated with the pretreated cells to evaluate their cellular uptake and interaction with the nanoconjugates.

Subcellular Distribution of RM@PLGA

T24 and 5637 cells were seeded into laser confocal dishes (1×10^5 cells per dish) and incubated for 12 h. Biotinylated R11 and streptavidin-biotin-PEG-modified M@PLGA-cou6 (coumarin-6, 2 mg/mL) were subsequently incubated with the cells. Organelles were stained with Lyso, ER and GA Tracker, respectively, using red fluorescence.

In vitro Cytotoxicity Assay

T24 and 5637 cells were seeded in 96-well plates at 8000 cells per well and incubated for 12 h. Then, the cells were treated with Gem, PLGA-Gem, M@PLGA-Gem, or RM@PLGA-Gem under various concentrations for 24 and 48h. Cytotoxicity was subsequently assessed using a CCK-8 assay.

Transwell and Wound-Healing Assay

T24 and 5637 cells were incubated with the indicated treatments and assessed for migration and invasion capabilities via Transwell and wound-healing assays. For Transwell assays, cells (5×10^5 per well) were seeded into the upper chambers of Transwell inserts (8.0 μm pore size, polyester membrane), while the lower chambers contained complete medium. After 24 h, non-migrating cells on the upper surface were removed with a cotton swab, and migrated cells on the lower surface were fixed with 4% paraformaldehyde, stained with 0.1% crystal violet, and counted under an inverted microscope. For wound-healing assays, cells were seeded in 6-well plates (8×10^5 per well) and cultured to confluence. A sterile pipette tip was used to create a uniform wound, and cells were treated as indicated. Wound closure was quantified by measuring the reduction in wound width at 24 and 48 h using phase-contrast microscopy.

In vitro Antitumor Treatment

T24 and 5637 cells were seeded in 6-well plates at a density of 2×10^5 cells per well and incubated for 24 h. Cells were then treated with the indicated formulations. For flow cytometric analysis, cells were suspended in PBS (pH 7.4) and analyzed using a flow cytometer. For cell cycle analysis, cells from both the supernatant and adherent layers were collected, fixed, and stained with propidium iodide. Apoptosis rates were determined using an annexin V/PI assay according to the manufacturer's protocol. T24 tumor spheroids (TSs) were prepared as previously described.[24] For penetration efficiency studies, TSs were incubated with RM@PLGA-cou6, PLGA-cou6, or M@PLGA-cou6 for 2 h, followed by washing and imaging using CLSM. Penetration depth was quantified using ImageJ software. For viability assays, TSs were treated as indicated, stained with calcein-AM (green, viable cells) and propidium iodide (red, dead cells), and imaged by CLSM following the manufacturer's instructions.

The in-vivo Studies Using Animal Model

The animal experiments were approved by the Laboratory Animal Management Committee at Zhejiang Provincial People's Hospital (20240605085754648534) and performed in accordance with the guidelines of the Administration Committee of Experimental Animals in Zhejiang Province and the Ethics Committee of Zhejiang Provincial People's Hospital. Female nu/nu mice (6–8 weeks old) were anesthetized with 1% isoflurane and maintained on a heated platform during catheterization. The bladder was flushed with sterile PBS, and a single-cell suspension of 5×10^5 GFP-transfected T24 cells in 100 μL of PBS was instilled into the bladder for 1 h to establish orthotopic bladder tumors. For targeting and penetration studies, biotinylated R11 was administered intravesically for 45 min, followed by incubation with streptavidin-biotin-PEG-modified M@PLGA labeled with coumarin-6 for 2 h. In therapeutic studies, various Gem formulations (10 mg/kg) were administered intravesically and retained for 2 h, with saline used as the control. Mice underwent treatment every 5 days for a total of five sessions. Tumor bioluminescence was monitored using the IVIS Spectrum system after intraperitoneal injection of D-luciferin (100 mg/kg). One day after the final treatment, mice were euthanized, and tissues were collected for H&E staining and imaging.

Results and Discussion

Tumor-selective mucoadhesive hydrogel was prepared as depicted in Figure 1A and B. The gelling properties of hydrogels composed of biotinylated R11 (R11-biotin) and M@PLGA-Gem (streptavidin-biotin-PEG modified) are shown in Figure 2A. M@PLGA-Gem, labeled with coumarin-6 or unlabeled, existed in a sol state but transitioned to a gel state upon exposure to R11-biotin (Figure 2A). The elastic modulus (G′) was largely independent of frequency (ω) and exceeded the viscous modulus (G″), indicative of typical gel behavior (Figure 2B). The bio-adhesion was demonstrated by the tensile strength required to disrupt the binding between bladder tissues and the hydrogel, as illustrated in the model depicted in Figure 2C. Briefly, tumor tissue sections were affixed to a wooden board, with the upper board connected to a plastic beaker via a fine thread. The beaker was filled with water to different volumes, providing gravitational force to attempt separation of the two boards. The threshold water volume in the beaker indicated the adhesive force between RM@PLGA-Gem and the luminal surface of bladder tissues, which was estimated to be 2606 ± 20 mN/cm², approximately 1.7-fold stronger than that of other gel formulations previously used in vaginal applications.[25]

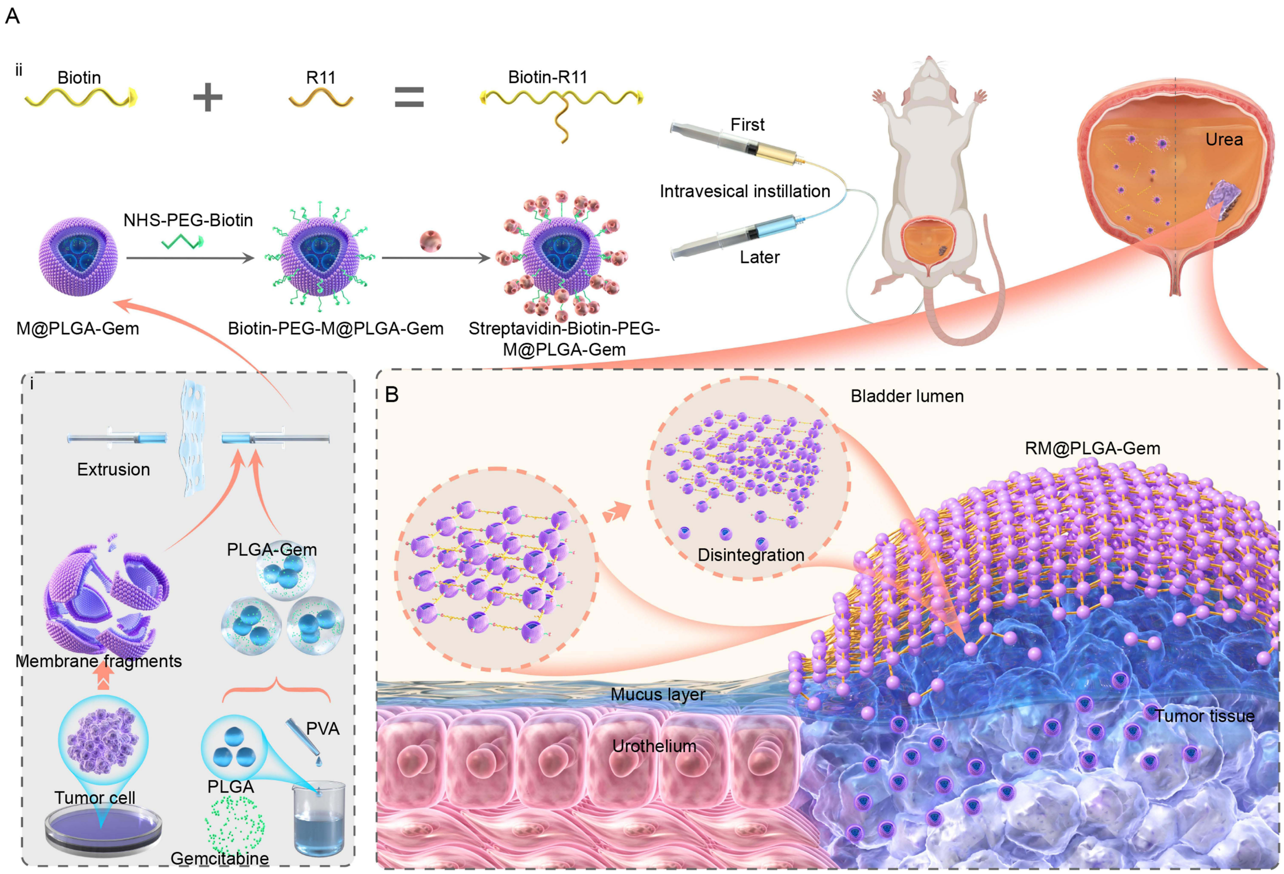

Figure 1 A tumor-selective and mucoadhesive hydrogel for the intravesical chemotherapy of BCa. (**A**) i. Gemcitabine-loaded PLGA nanoparticles and cell membrane fragments were co-extruded through liposome-extruder to form membrane-coated nanoparticles (MN); ii. MN were further surface engineered with streptavidin-biotin-PEG. Sequential Intravesical Delivery of R11-Biotin and streptavidin-Biotin-PEG Modified M@PLGA-Gem. (**B**) Following intravesical administration, R11-biotin and streptavidin-biotin-PEG modified M@PLGA-Gem undergo self-assembly into a hydrogel on the surface of BCa, effectively creating a nano-drug reservoir that enhances retention time. The hydrogel then gradually degrades, releasing M@PLGA-Gem, thereby achieving targeted therapy for BCa.

DLS analysis revealed that the zeta potentials of PLGA-Gem and M@PLGA-Gem were −2.6 ± 0.29 mV and −14.1 ± 1.2 mV, respectively (Figure 2D). The average particle diameters of PLGA-Gem in urine, M@PLGA-Gem in urine, PLGA-Gem in PBS buffer, and M@PLGA-Gem in PBS buffer were 201.3 ± 0.8 nm, 226.2 ± 1.2 nm, 190.6 ± 0.5 nm, and 224.0 ± 0.5 nm, respectively (Figure 2E). Despite the complex, hypotonic, and acidic nature of urine, which can compromise nanoparticle stability, M@PLGA-Gem nanoparticles demonstrated high stability in both PBS buffer (pH 7.4) and urine, with no significant changes in zeta potential or particle size (Figure 2E and F). The drug loading content (DLC) of Gem in PLGA nanoparticles was calculated to be 16.5%, with a drug loading efficiency (DLE) of 92.5%. SEM imaging (Figure 2G) showed that M@PLGA-Gem nanoparticles exhibited a spherical morphology, primarily ranging in size from 200 to 250 nm. The disintegration of the hydrogel in PBS buffer or urine was monitored over 48 h, with 60% and 75% degradation observed in PBS and urine, respectively (Figure S1). The cumulative release of Gem from PLGA-Gem, M@PLGA-Gem, and RM@PLGA-Gem after 48 h of incubation in urine was 70.6 ± 1.2%, 46.7 ± 1.7%, and 32.1 ± 0.5%, respectively (Figure 2H). The more controlled release of Gem from RM@PLGA-Gem is attributed to the gradual disintegration of the hydrogel shell. The mucus-penetrating efficiency of coumarin-6 (used in place of Gem for better detection) was evaluated using a Transwell diffusion chamber with a chondroitin sulfate-coated insert, which mimics the impermeability of the mucus layer. The transmucosal transport of coumarin-6 delivered via RM@PLGA-cou6 was the most rapid over 6 h, resulting in 1.7-fold and 1.4-fold greater transport (46.0 ± 0.6%) compared to PLGA-cou6 and M@PLGA-cou6, respectively (Figure 2I). This enhanced mucus-penetrating ability of RM@PLGA-cou6 is likely due to electrostatic neutralization between positively charged R11 and negatively charged chondroitin sulfate in the mucus layer, facilitating transmucosal transport of the nanovesicles.

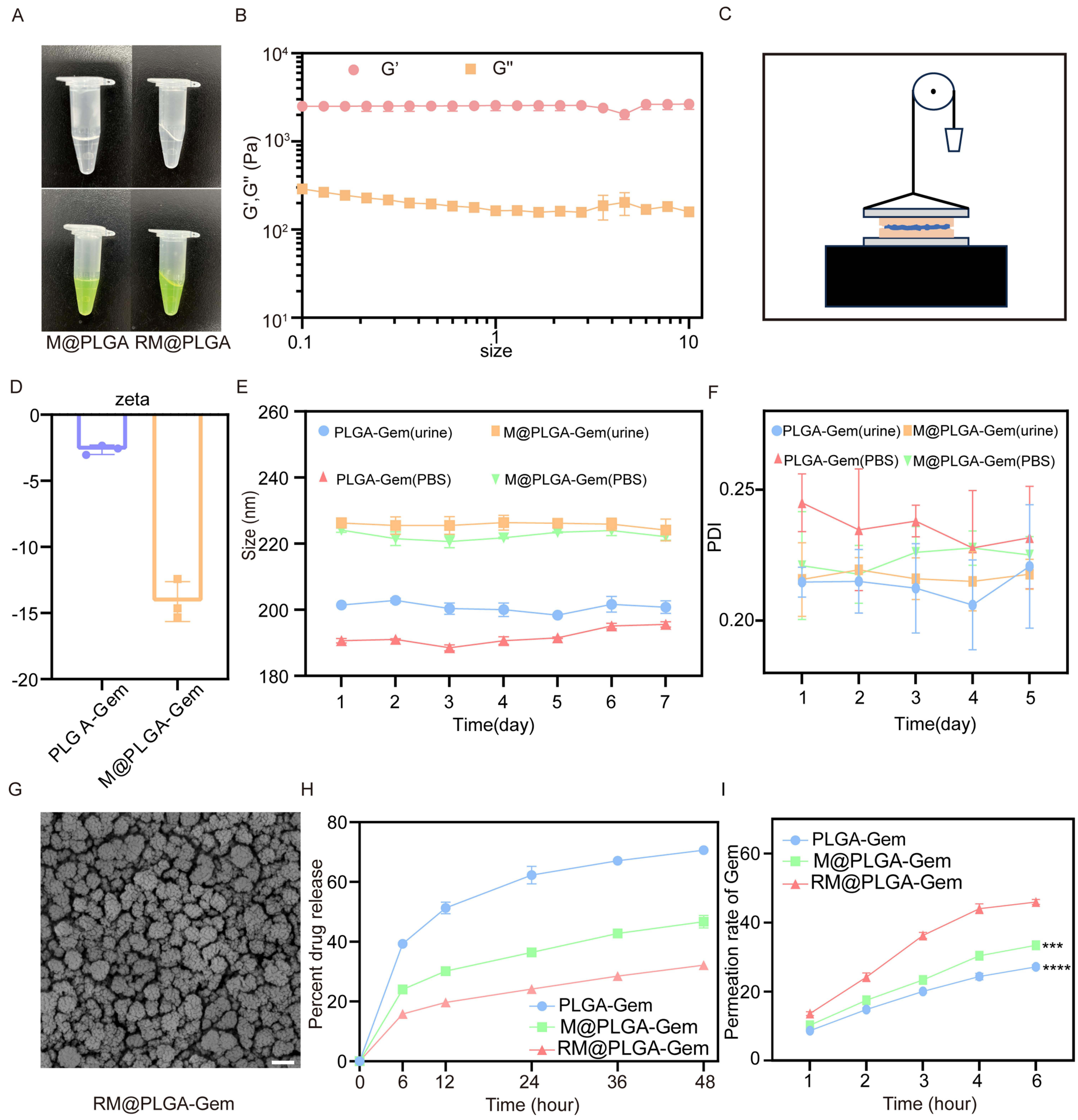

Figure 2 Physicochemical properties of nanoparticles and hydrogels. (**A**) Representative photographs of the sol and the gel states. (**B**) Dynamic rheology of RM@PLGA-Gem. (**C**) The scheme of the device used in the measurement of mucoadhesive force. (**D**) The average zeta potential of PLGA-Gem and M@PLGA-Gem. (**E**) The stability of the size of PLGA-Gem and M@PLGA-Gem. (**F**) The change of the polydispersity index PLGA-Gem, M@PLGA-Gem, PLGA-Gem (Urine) and M@PLGA-Gem (Urine) after timed incubation. (**G**) SEM image of RM@PLGA-Gem. Scar bar: 2 μm. (**H**) Drug release profiles of Gem (Gem-eq dose: 20 μg/mL) from PLGA-Gem, M@PLGA-Gem and RM@PLGA-Gem. (**I**) GAG layer permeation assay. For convenience of quantification, Gem was replaced with coumarin-6. *** $p < 0.001$, **** $p < 0.0001$.

The tumor-selective gelation followed a two-step pre-targeting strategy. R11-biotin, serving as the tumor-targeting component, undergoes stable cell membrane insertion, achieving equilibrium between endocytosis and membrane binding. The endocytic dynamics of R11-biotin in T24 cells were evaluated at five-minute intervals (Figure S2), with peak uptake observed after 45 minutes of coincubation. The tumor-selective gelation, activated by sequential administration of R11-biotin and streptavidin-biotin-PEG-modified M@PLGA, was tested in SVHUC-1, T24, and 5637 cells, as well as their tumor spheroid (TS) counterparts. Hydrogel formation occurred only when the solid content exceeded a 5% (w/v) threshold. Under these conditions, SVHUC-1 cells, representing normal urothelial cells, showed no surface deposition of the hydrogel, whereas tumor cells (T24 and 5637) were coated with a thick, mist-like hydrogel layer (Figure 3A and B). Blocking the binding sites of R11-conjugated biotin with excess streptavidin prevented its interaction with streptavidin-biotin-PEG-modified M@PLGA-cou6. Sequential use of streptavidin-blocked R11-biotin and M@PLGA-cou6 failed to induce tumor-selective hydrogel formation on either cell surfaces or TS surfaces (Figure S3A and B). Collectively, these results confirm the successful achievement of tumor-selective gelation through the pre-targeting strategy.

The disintegration of the hydrogel on the tumor surface is essential for the rapid release of Gem into tumor cells. To facilitate observation, Gem was replaced with coumarin-6 in RM@PLGA-Gem (RM@PLGA-cou6). The self-disintegrating properties of RM@PLGA-cou6 at the tumor surface were evaluated using a Transwell diffusion model. In this model, tumor cells were densely seeded in the upper chamber, with the hydrogel positioned above and the lower chamber filled with PBS buffer or urine to mimic the tumor microenvironment. At regular

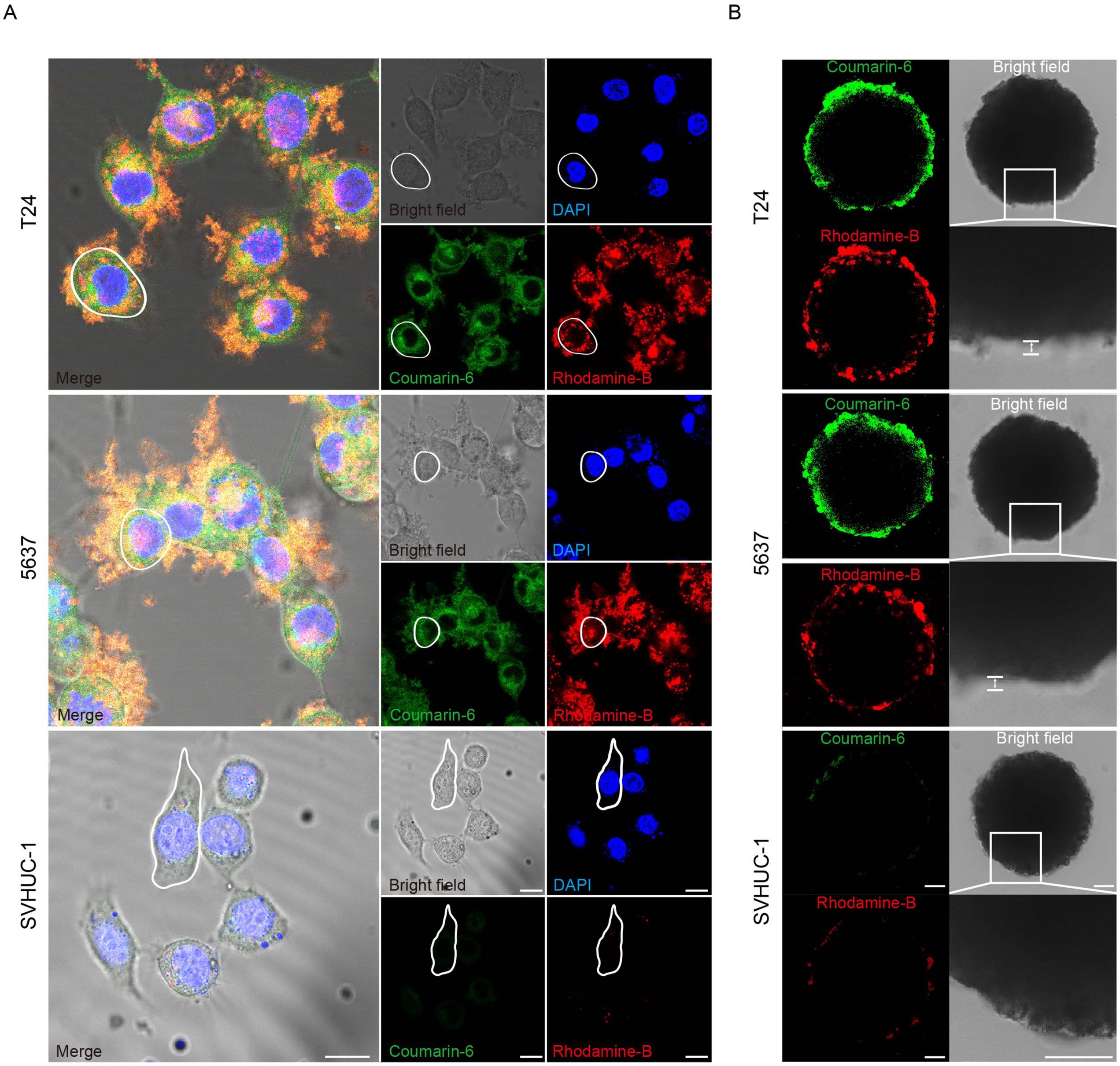

Figure 3 Tumor surface-specific gelation. (**A**) Confocal images of T24, 5637 and SVHUC-1 stained with Hoechst (nuclei, blue), R11 (Rhodamine-B, Red) and membrane-coated nanoparticles (coumarin-6, Green) in the RM@PLGA-cou6 group. Scar bar: 20 μm. (**B**) Confocal images of T24, 5637 and SVHUC-1 TSs stained with R11 (Rhodamine-B, Red) and membrane-coated nanoparticles (coumarin-6, Green) in the RM@PLGA-cou6 group. Scar bar: 50 μm.

https://doi.org/10.2147/IJN.S522421

intervals, the hydrogel was scratched, and the remaining coumarin-6, representing the unreleased fraction, was collected for fluorescence quantification. The results showed that after 24 h of exposure to urine and PBS buffer, 33.2 ± 2.1% and 32.4 ± 1.5% (T24) and 24.0 ± 2.5% and 22.7 ± 2.0% (5637) of coumarin-6 were released from the hydrogel, respectively (Figure S4). The degradation of the hydrogel adhered to T24/5637 tumor spheroids (TSs) was visualized by reduced hydrogel thickness, with 68.8 ± 1.5% (T24) and 67.0 ± 0.8% (5637) of the hydrogel breaking down after 24 h of incubation. The distribution of coumarin-6 within the TSs, indicative of the released fraction from the inner hydrogel layer, penetrated the TSs in a time-dependent manner (Figure 4A–D).

As shown in Figure S5A and B, the fluorescence intensity of coumarin-6 in T24 and 5637 cells exhibited an 8.8 ± 0.2-fold and 8.6 ± 0.1-fold enhancement, respectively, compared to SVHUC-1 cells following treatment with RM@PLGA-cou6. Flow cytometric analysis confirmed the tumor-selective internalization of coumarin-6 (Figure S6). Mechanistic studies revealed that only filipin and low-temperature conditions specifically inhibited the endocytosis of RM@PLGA-cou6 in T24 and 5637 cells,[26–28] thereby establishing the energy-dependent and caveolin-mediated pathway responsible for nanoparticle internalization (Figure 5A and B). This observation aligns with prior reports indicating that clathrin-mediated endocytosis directs cargo to lysosomes, while caveolae-mediated endocytosis facilitates lysosome-independent trafficking.[29,30] Intracellular trafficking analysis via CLSM demonstrated strong colocalization of RM@PLGA-cou6 with the ER and GA, whereas minimal overlap was observed with lysosomes (Figure 5C and D). The tumor-penetrating capacity of coumarin-6-loaded nanoparticles was evaluated in TSs.[31] Gem was replaced by coumarin-6 in different treatments. While PLGA-cou6 and M@PLGA-cou6 nanoparticles were restricted to the peripheral layers of TSs, RM@PLGA-cou6 exhibited deep penetration into the inner regions of T24 TSs, nearly achieving uniform distribution throughout the spheroid. This resulted in a 5.3-fold and 4.3-fold higher coumarin-6 fluorescence intensity in RM@PLGA-cou6-treated groups compared to PLGA-cou6- and M@PLGA-cou6-treated groups, respectively (Figures 5E–G and S7). Collectively, these findings highlight RM@PLGA-cou6 as a promising platform for tumor-selective and deep-penetrating drug delivery.

The inhibitory effects of all Gem formulations on T24 cell proliferation were time- and concentration-dependent. Notably, RM@PLGA-Gem exhibited the most profound antitumor activity, as evidenced by its ability to reduce cell viability to 40.3 ± 2.0% at a Gem-equivalent dose of 10 µg/mL after 24 h of treatment (Figure 6A and B). These findings are in agreement with prior studies demonstrating that RM@PLGA-Gem induces cell cycle arrest at the S phase (Figure S8A and B) and promotes late apoptosis (Figure S9A and B). Furthermore, RM@PLGA-Gem exhibited the most pronounced inhibitory effect on cell migration, as characterized by scratch wound healing and Transwell migration assays (Figures 6C, 6D, S10 and S11A–C). In TSs models, RM@PLGA-Gem induced significantly greater cell death compared to PLGA-Gem and M@PLGA-Gem (Figures 7 and S12), highlighting its superior efficacy in a 3D tumor environment.

The murine orthotopic BCa model is widely recognized as a robust platform for evaluating the in vivo behavior of intravesical agents.[32–35] In this study, RM@PLGA-Gem demonstrated the unique ability to form a hydrogel at the tumor cap within the bladder lumen, without spreading to normal urothelium. In contrast, PLGA-Gem and M@PLGA-Gem exhibited non-selective adherence to the luminal surface without specific tumor targeting (Figures 8 and S13). Comparative analysis of the antitumor efficacy of various Gem formulations revealed that RM@PLGA-Gem exhibited the most pronounced antitumor activity. It not only potently suppressed tumor growth during the initial intravesical (IT) treatment phase but also completely eradicated tumors in all treated mice by the end of the study, with no recurrence observed over a 25-day follow-up period. The antitumor effects of M@PLGA-Gem and PLGA-Gem were modest but still superior to free Gem (Figure 9A and B). Specifically, the tumor inhibition rate for RM@PLGA-Gem reached 100%, compared to 53.7% for M@PLGA-Gem and 30.7% for PLGA-Gem. Mice in groups with delayed tumor progression exhibited steady weight gain, whereas significant weight loss was observed in groups with progressive disease following the metaphase of intravesical therapy (Figure 9C). Histopathological examination of major organs (heart, liver, spleen, lung, and kidney) via hematoxylin and eosin (H&E) staining revealed no significant pathological changes across all

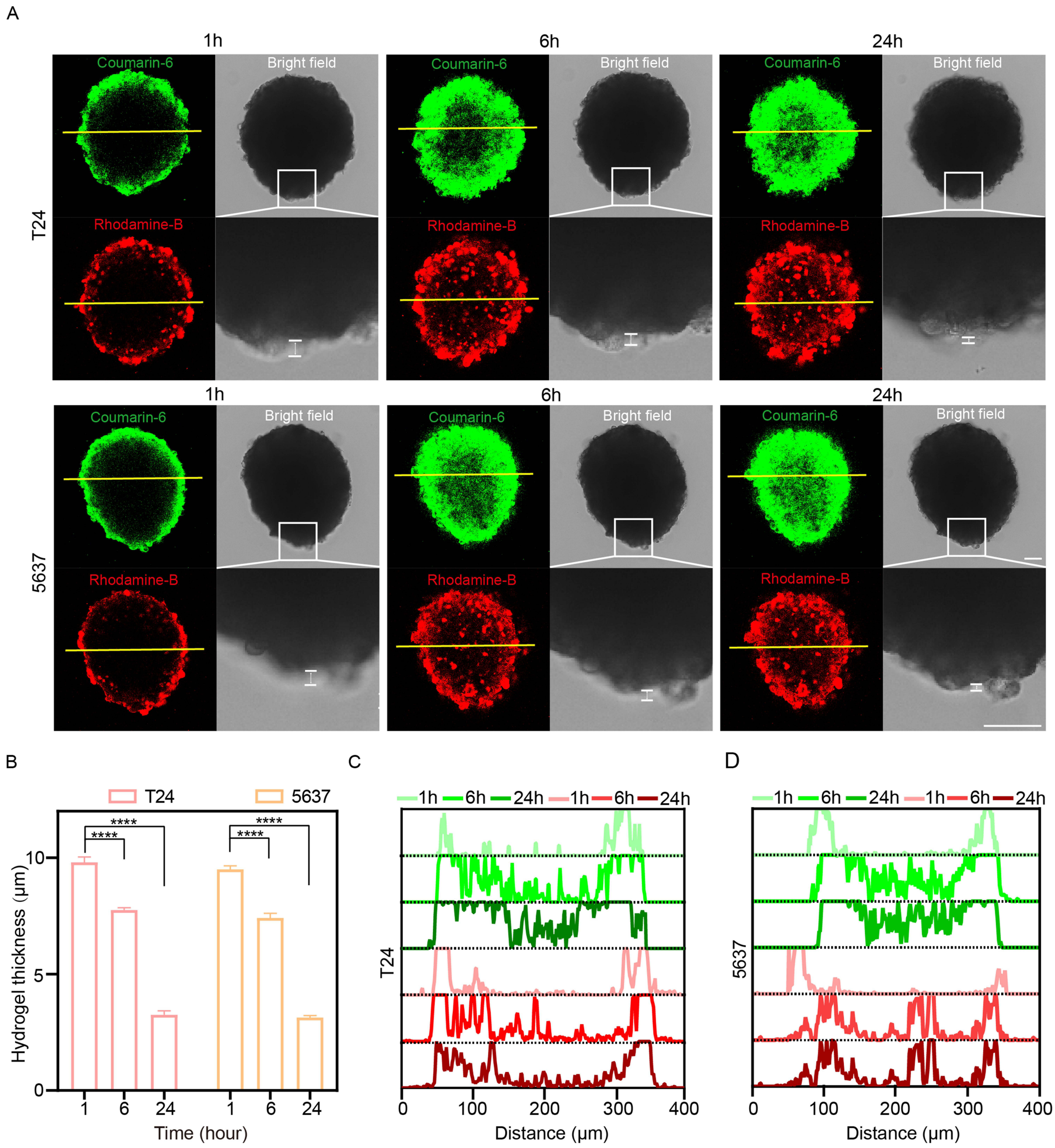

Figure 4 Decomposition of the hydrogel on the tumor surface. (**A**) Confocal images of the degradation of tumor surface-specific hydrogel on the surfaces of T24 and 5637 TSs (R11, Rhodamine-B; Membrane-coated nanoparticles, coumarin-6). (**B**) Thickness of hydrogels on the surface of T24 and 5637 TSs for different times. (**C**) The distribution of T24 TSs along the yellow line indicated in (Figure S4) for different times, as demonstrated by Coumarin 6 fluorescence. (**D**) The distribution of 5637 TSs along the yellow line indicated in (Figure S4) for different times, as demonstrated by Coumarin 6 fluorescence. Scar bar: 50 μm. **** $p < 0.0001$.

treatment groups (Figure 9D). Notably, orthotopic BCa was undetectable in mice treated with RM@PLGA-Gem, whereas residual tumors persisting in other treatment groups exhibited invasion into the muscular layers. Additionally, no signs of liver or renal dysfunction attributable to intravesical therapy were observed in any group (Figure 9E). These findings collectively underscore the superior therapeutic profile and safety of RM@PLGA-Gem for intravesical BCa treatment.

https://doi.org/10.2147/IJN.S522421

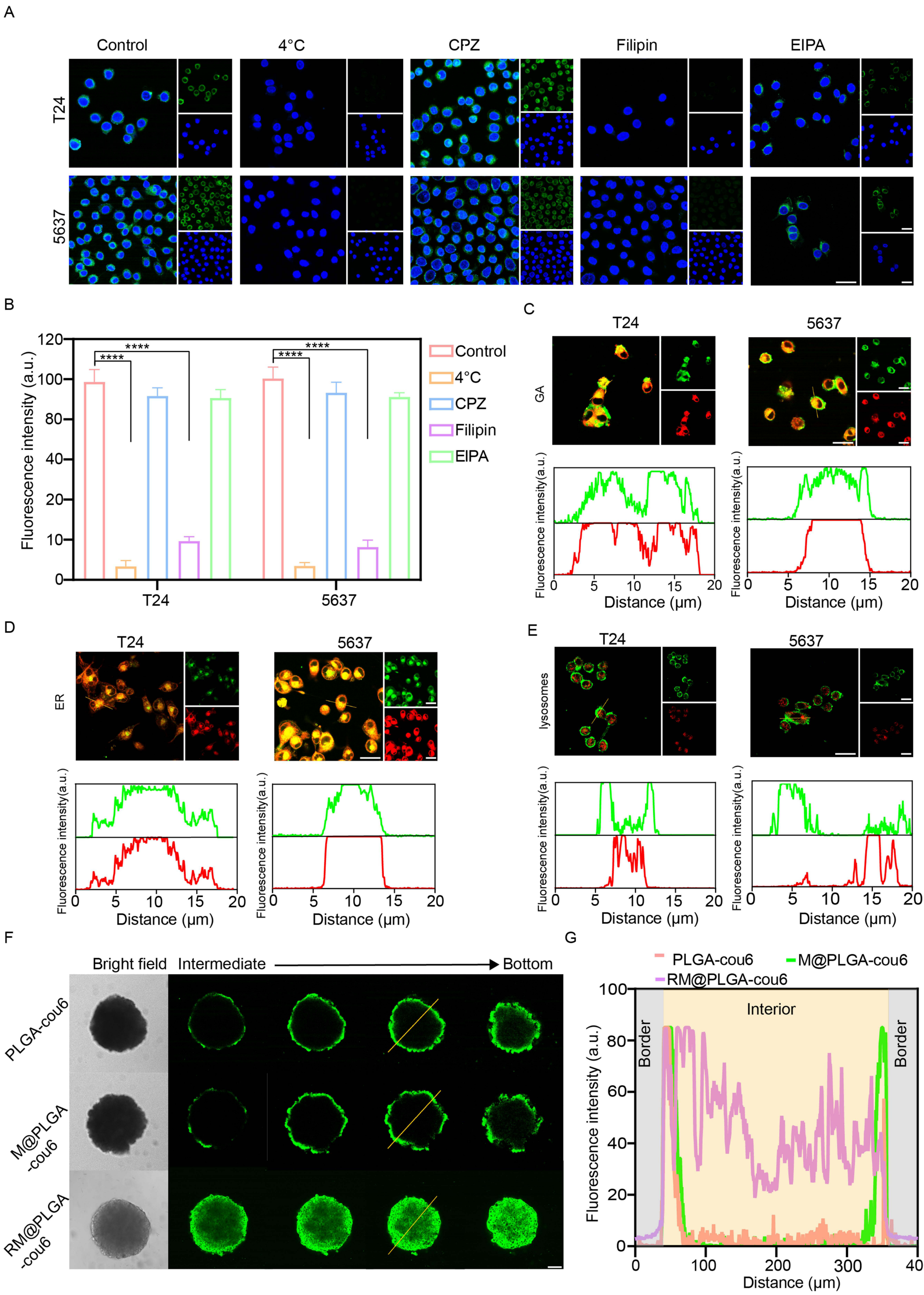

Figure 5 The BCa endocytosis pathway, intracellular trafficking fate and penetration efficiency in tumor spheroids. (**A**) CLSM analysis of the endocytosis inhibition by different treatments; scale bar: 25 μm. (**B**) Statistical analysis of the endocytosis inhibition by different treatments. (**C**) The subcellular colocalization of RM@PLGA-cou6 (Gem is replaced by coumarin-6) and GA; Green: RM@PLGA-cou6; Red: GA tracker; scale bar: 25 μm. (**D**) The subcellular colocalization of RM@PLGA-cou6(Gem is replaced by coumarin-6) and ER; Green: RM@PLGA-cou6; Red: ER tracker; scale bar: 25 μm. (**E**) The subcellular colocalization of RM@PLGA-cou6(Gem is replaced by coumarin-6) and lysosomes; Green: RM@PLGA-cou6; Red: lysotracker; scale bar: 25 μm. (**F**) The ability of different treatments to penetrate the urothelium in T24 TSs. Gem is replaced by coumarin-6 in different treatments. The Z-stack analysis spanned from the intermediate layer to the bottom layer at 100 μm intervals; Scale bar, 100 μm. (**G**) The distribution of various treatments within T24 TSs along the yellow line indicated in (F), as demonstrated by Coumarin 6 fluorescence. **** $p < 0.000.1$.

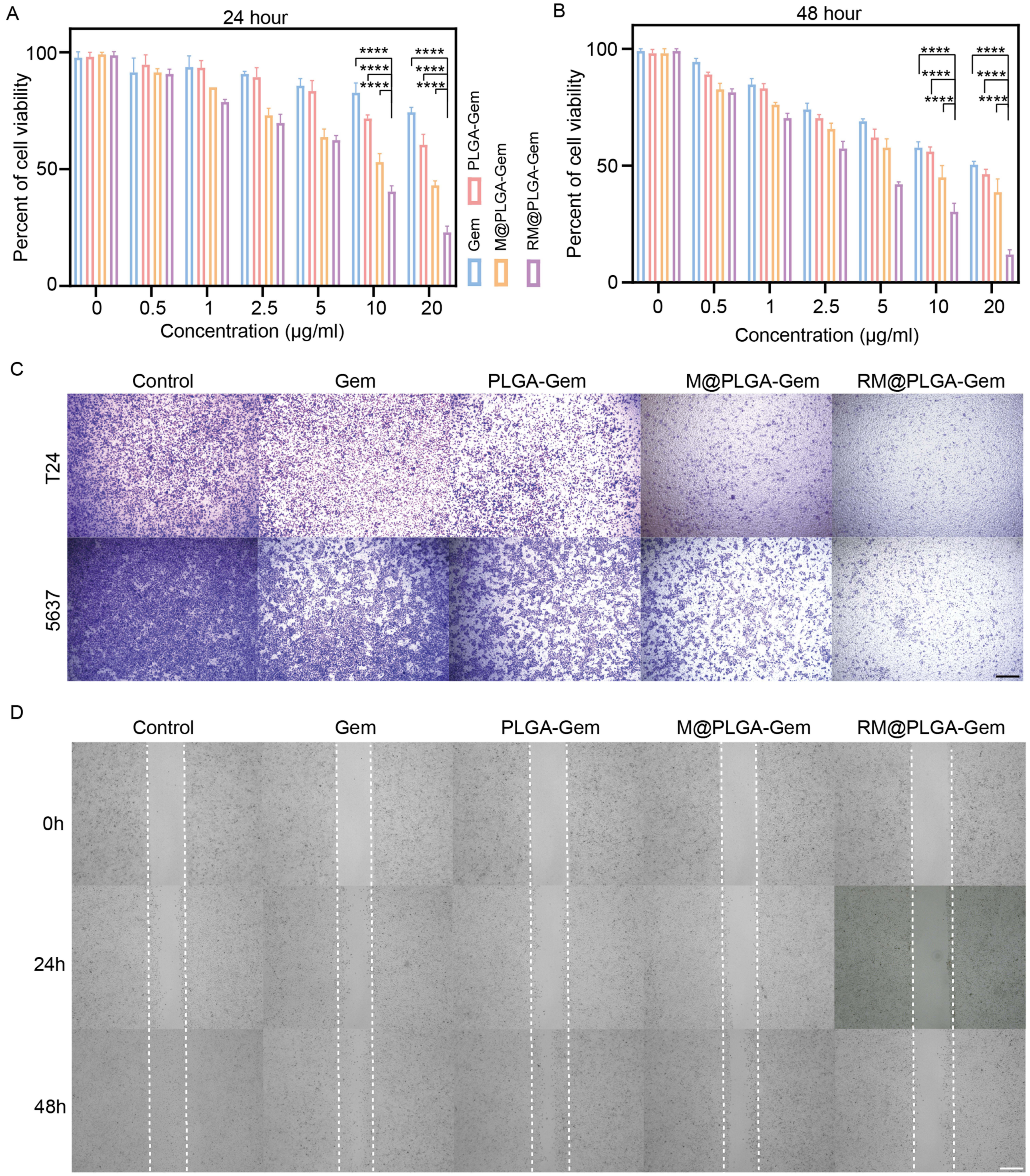

Figure 6 In vitro anticancer activity. (**A**) Cytotoxicity of different treatments for 24 h incubation. (**B**) Cytotoxicity of different treatments for 48 h incubation. (**C**) Effect of different treatments on T24 cell migration as detected by Transwell assay; scale bar: 200 μm. (**D**) Effect of different treatments on T24 and 5637 cells migration as determined by scratch wound healing assay; scale bar: 200 μm. **** $p < 0.0001$.

Conclusion

In summary, we employed a pretargeting strategy to develop a mucoadhesive and tumor-selective hydrogel for intravesical therapy of BCa. This strategy involved a two-step intravesical delivery system comprising R11-biotin and hydrogel precursors. Our findings demonstrated that the mucoadhesive TsH significantly enhanced both the intravesical

https://doi.org/10.2147/IJN.S522421

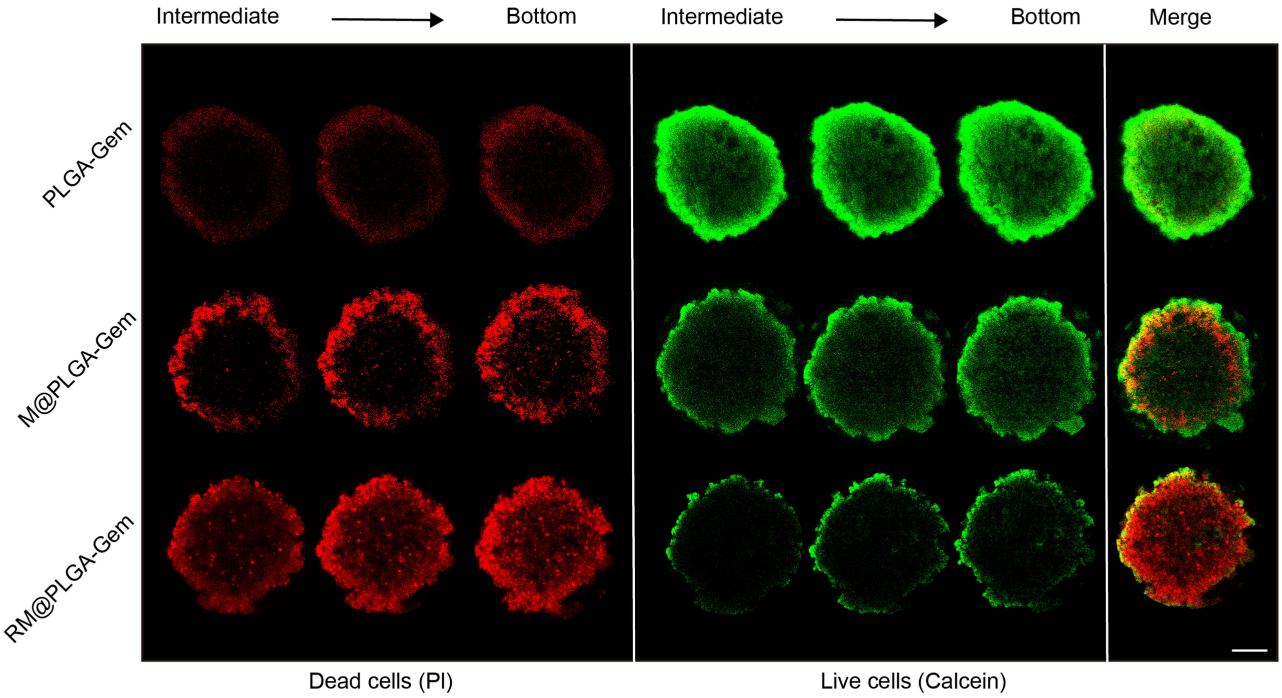

Figure 7 Fluorescent images of T24 TSs in different groups with Live/Dead staining (viable cells are stained green fluorescence with Calcein-AM and dead ones are stained red fluorescence with PI). Scar bar: 100 µm.

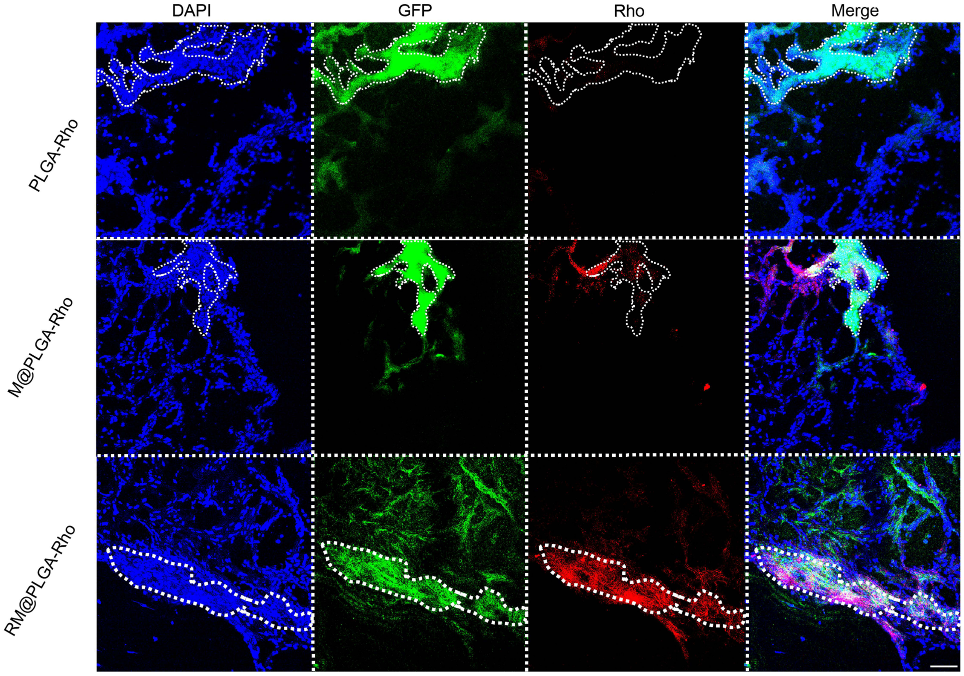

Figure 8 Tumor-selective targeting. The colocalization of coumarin-6-labeled different treatments and GFP-labeled tumor regions after a single intravesical instillation in murine orthotopic BCa models. Gem is replaced by Rhodamine B in different treatments; Scar bar: 100 µm.

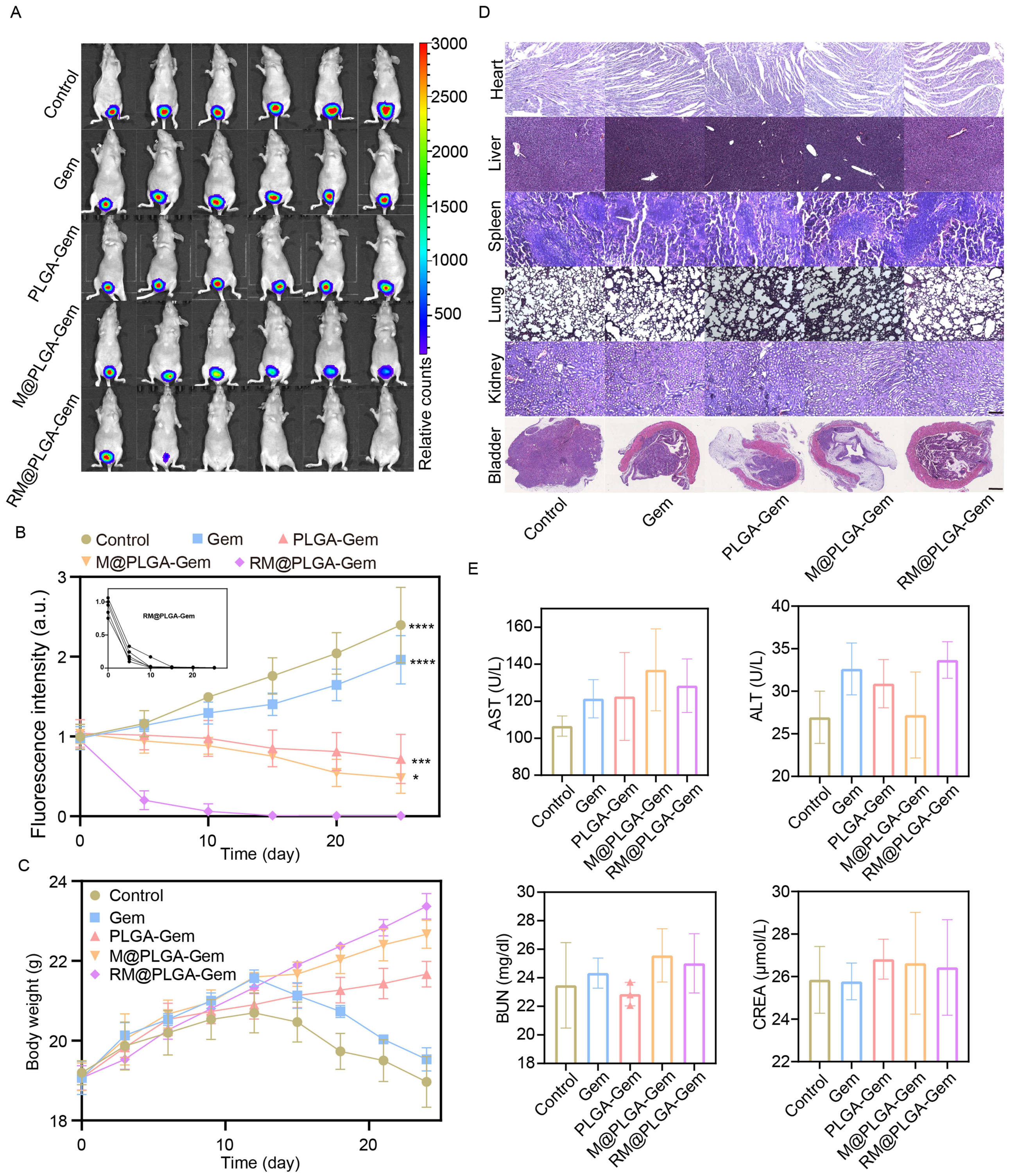

Figure 9 Anti-tumor effect of hydrogel in murine orthotopic BCa models. (**A**) In vivo bioluminescence imaging was used to assess the anti-tumor efficacy of various Gem formulations against orthotopic T24-Luci bladder cancer. (**B**) Changes in the average bioluminescence intensity of orthotopic bladder cancer across different groups during intravesical therapy are depicted. The inset illustrates the individual bioluminescence intensity changes in orthotopic bladder cancer in mice treated with RM@PLGA-Gem. (**C**) Variations in the average body weight of mice in different groups during intravesical therapy are shown. (**D**) Histopathological examination of normal organs and bladder tissues in different groups. Scale bar: 200 μm (normal organs), Scale bar: 1 mm (bladders). (**E**) Biochemical analysis of blood samples from different groups. * $p < 0.05$, *** $p < 0.001$, **** $p < 0.0001$.

retention and tumor-selective distribution of Gem. Notably, the intravesically delivered Gem via TsH effectively achieved chemo-resection of bladder tumors in the majority of cases. These preclinical data provide compelling evidence supporting the mucoadhesive TsH as a promising platform for intravesical BCa therapy, warranting further exploration for clinical translation.

Acknowledgments

The authors are thankful to the National Natural Science Foundation of China (82300868, 82473503) for funding this work.

Disclosure

The authors report no conflicts of interest in this work.

References

1. Kobayashi T, Owczarek TB, McKiernan JM, Abate-Shen C. Modelling bladder cancer in mice: opportunities and challenges. *Nat Rev Cancer*. 2015;15(1):42–54. doi:10.1038/nrc3858
2. Antoni S, Ferlay J, Soerjomataram I, Znaor A, Jemal A, Bray F. Bladder cancer incidence and mortality: a global overview and recent trends. *Eur Urol*. 2017;71(1):96–108. doi:10.1016/j.eururo.2016.06.010
3. Davis RM, Kiss B, Trivedi DR, Metzner TJ, Liao JC, Gambhir SS. Surface-enhanced raman scattering nanoparticles for multiplexed imaging of bladder cancer tissue permeability and molecular phenotype. *ACS Nano*. 2018;12(10):9669–9679. doi:10.1021/acsnano.8b03217
4. Neutsch L, Eggenreich B, Herwig E, et al. Lectin bioconjugates trigger urothelial cytoinvasion--a glycotargeted approach for improved intravesical drug delivery. *Eur J Pharm Biopharm*. 2012;82(2):367–375. doi:10.1016/j.ejpb.2012.07.016
5. GuhaSarkar S, Banerjee R. Intravesical drug delivery: challenges, current status, opportunities and novel strategies. *J Control Release*. 2010;148 (2):147–159. doi:10.1016/j.jconrel
6. Babjuk M, Böhle A, Burger M, et al. EAU guidelines on non-muscle-invasive urothelial carcinoma of the bladder: update 2016. *Eur Urol*. 2017;71 (3):447–461. doi:10.1016/j.eururo.2016.05.041
7. Gasión JP, Cruz JF. Improving efficacy of intravesical chemotherapy. *Eur Urol*. 2006;50(2):225–234. doi:10.1016/j.eururo.2006.05.035
8. Joice GA, Bivalacqua TJ, Kates M. Optimizing pharmacokinetics of intravesical chemotherapy for bladder cancer. *Nat Rev Urol*. 2019;16 (10):599–612. doi:10.1038/s41585-019-0220-4
9. Lingyun Z, Fengting L, Libing L, Shu W. Post-expansile hydrogel foam aerosol of PG-liposomes: a novel delivery system for vaginal drug delivery applications. *CCS Chem*. 2019;1:97–105. doi:10.1016/j.ejps.2012.06.001
10. Zhang R, Song X, Liang C, et al. Catalase-loaded cisplatin-prodrug-constructed liposomes to overcome tumor hypoxia for enhanced chemo-radiotherapy of cancer. *Biomaterials*. 2017;138:13–21. doi:10.1016/j.biomaterials.2017.05.025
11. Niu D, He J, Qin X, et al. Superstable and large-scalable organosilica-micellar hybrid nanosystem via a confined gelation strategy for ultrahigh-dosage chemotherapy. *Nano Lett*. 2021;21(22):9388–9397. doi:10.1021/acs.nanolett.1c02342
12. Yuan Z, Pan Y, Cheng R, et al. Doxorubicin-loaded mesoporous silica nanoparticle composite nanofibers for long-term adjustments of tumor apoptosis. *Nanotechnology*. 2016;27(24):245101. doi:10.1088/0957-4484/27/24/245101
13. Xu X, Liu K, Jiao B, et al. Mucoadhesive nanoparticles based on ROS activated gambogic acid prodrug for safe and efficient intravesical instillation chemotherapy of bladder cancer. *J Control Release*. 2020;10(324):493–504. doi:10.1016/j.jconrel.2020.03.028
14. Zhang Z, Ai S, Yang Z, Li X. Peptide-based supramolecular hydrogels for local drug delivery. *Adv Drug Deliv Rev*. 2021;174:482–503. doi:10.1016/j.addr.2021.05.010
15. Babjuk M, Burger M, Compérat EM, et al. European association of urology guidelines on non-muscle-invasive bladder cancer (TaT1 and carcinoma in situ) - 2019 update. *Eur Urol*. 2019;76(5):639–657. doi:10.1016/j.eururo.2019.08.016
16. Zhou XY, Wang CK, Shen ZF, et al. Recent research progress on tumour-specific responsive hydrogels. *J Mater Chem B*. 2024;12(30):7246–7266. doi:10.1039/d4tb00656a
17. Vago R, Radano G, Zocco D, Zarovni N. Urine stabilization and normalization strategies favor unbiased analysis of urinary EV content. *Sci Rep*. 2022;12(1):17663. doi:10.1038/s41598-022-22577-3
18. Maalouf NM, Cameron MA, Moe OW, Adams-Huet B, Sakhaee K. Low urine pH: a novel feature of the metabolic syndrome. *Clin J Am Soc Nephrol*. 2007;12(2):883–888. doi:10.2215/CJN.00670207
19. Valko M, Leibfritz D, Moncol J, Cronin MT, Mazur M, Telser J. Free radicals and antioxidants in normal physiological functions and human disease. *Int J Biochem Cell Biol*. 2007;39(1):44–84. doi:10.1016/j.biocel.2006.07.001
20. Chen X, Liu Z. A pH-responsive hydrogel based on a tumor-targeting mesoporous silica nanocomposite for sustained cancer labeling and therapy. *Macromol Rapid Commun*. 2016;37(11):1533–1539. doi:10.1002/marc.201600261
21. Hodson AW. Separation of alkaline phosphatase isoenzymes from human kidney and comparison with alkaline phosphatases from other human tissues, urine, and Escherichia coli. *Clin Chem*. 1983;29(1):100–106. doi:10.1093/clinchem/29.1.100
22. Yang X, Gao S, Yang B, et al. Bioinspired tumor-targeting and biomarker-activatable cell-material interfacing system enhances osteosarcoma treatment via biomineralization. *Adv Sci*. 2023;10(1):e2302272. doi:10.1002/advs.202302272
23. Thompson MS, Tsurkan MV, Chwalek K, et al. Self-assembling hydrogels crosslinked solely by receptor-ligand interactions: tunability, rationalization of physical properties, and 3D cell culture. *Chemistry*. 2015;21(12):3178–3182. doi:10.1002/chem.201406366
24. Zheng B, Liu Z, Wang H, et al. R11 modified tumor cell membrane nanovesicle-camouflaged nanoparticles with enhanced targeting and mucus-penetrating efficiency for intravesical chemotherapy for bladder cancer. *J Control Release*. 2022;351(23):834–846. doi:10.1016/j.jconrel.2022.09.055

25. Li WZ, Zhao N, Zhou YQ, et al. Post-expansile hydrogel foam aerosol of PG-liposomes: a novel delivery system for vaginal drug delivery applications. *Eur J Pharm Sci*. 2012;47(2):162–169. doi:10.1016/j.ejps.2012.06.001
26. Yılmaz D, Culha M. Investigation of the pathway dependent endocytosis of gold nanoparticles by surface-enhanced Raman scattering. *Talanta*. 2021;225(13):122071. doi:10.1016/j.talanta.2020
27. Caì Y, Postnikova EN, Bernbaum JG, et al. Simian hemorrhagic fever virus cell entry is dependent on CD163 and uses a clathrin-mediated endocytosis-like pathway. *J Virol*. 2015;89(1):844–856. doi:10.1128/JVI.02697-14
28. Nagai N, Ogata F, Otake H, Nakazawa Y, Kawasaki N. Energy-dependent endocytosis is responsible for drug transcorneal penetration following the instillation of ophthalmic formulations containing indomethacin nanoparticles. *Int J Nanomedicine*. 2019;14(8):1213–1227. doi:10.2147/IJN.S196681
29. Ehrlich M, Boll W, Van Oijen A, et al. Endocytosis by random initiation and stabilization of clathrin-coated pits. *Cell*. 2004;118(5):591–605. doi:10.1016/j.cell.2004.08.017
30. Nichols B. Caveosomes and endocytosis of lipid rafts. *J Cell Sci*. 2003;116(23):4707–4714. doi:10.1242/jcs.00840
31. Adema AD, Laan AC, Myhren F, et al. Inhibition of checkpoint kinase 1 potentiates anticancer activity of gemcitabine in bladder cancer cells. *Sci Rep*. 2021;11(10):10181–10188. doi:10.1038/s41598-021-89684-5
32. Zhou Q, Shao S, Wang J, et al. Enzyme-activatable polymer-drug conjugate augments tumour penetration and treatment efficacy. *Nat Nanotechnol*. 2019;14(8):799–809. doi:10.1038/s41565-019-0485-z
33. Doreen H, Christiane R, Ralf B, et al. An orthotopic xenograft model for high-risk non-muscle invasive bladder cancer in mice: influence of mouse strain, tumor cell count, dwell time and bladder pretreatment. *BMC Cancer*. 2017;17:790–802. doi:10.1186/s12885-017-3778-3
34. Roelants M, Van Cleynenbreugel B, Van Poppel H, Lerut E, de Witte PA. Use of fluorescein isothiocyanate-human serum albumin for the intravesical photodiagnosis of non-muscle-invasive bladder cancer: an in vitro study using multicellular spheroids composed of normal human urothelial and urothelial cell carcinoma cell lines. *BJU Int*. 2011;108(3):455–459. doi:10.1111/j.1464-410X.2010.09951.x
35. Vasyutin I, Zerihun L, Ivan C, Atala A. Bladder organoids and spheroids: potential tools for normal and diseased tissue modelling. *Anticancer Res*. 2019;39(3):1105–1118. doi:10.21873/anticanres.13219